RSC Advances

ROYAL SOCIETY OF CHEMISTRY

www.rsc.org/advances

One-dimensional barium titanate coated multi-walled carbon nanotube heterostructures: Synthesis and electromagnetic absorption properties

Yao-Feng Zhu [a,b*], Qing-Qing Ni[a], and Ya-Qin Fu[a]

[a] Key Laboratory of Advanced Textile Materials and Manufacturing Technology Ministry of Education, Zhejiang Sci-Tech University, Hangzhou 310018, P.R. China

[b] National Engineering Lab for Textile Fiber Materials and Processing Technology, Zhejiang Sci-Tech University, Hangzhou 310018, P.R. China

*Corresponding author. Tel.: Fax: +86 571 86843607. E-mail address: yfzhu@zstu.edu.cn (Y. F. Zhu);

Abstract

One-dimensional barium titanate ($BaTiO_3$) @ multi-walled carbon nanotube (MWCNT) core/shell heterostructure composites are prepared via a sol-gel route combined with a thermal treatment process. Field emission scanning electron microscopy and transmission electron microscopy measurements show that the $BaTiO_3$@MWCNT core/shell heterostructure composites have a $BaTiO_3$ film thickness of ~10 nm, and that the $BaTiO_3$ film uniformly encapsulates the surface of the MWCNT core. The measured electromagnetic parameters show that the $BaTiO_3$@MWCNT composites exhibit remarkable and improved electromagnetic wave absorption properties, compared to both pristine MWCNTs and $BaTiO_3$. Notably, more than 99% of electromagnetic wave energy can be attenuated by the $BaTiO_3$@MWCNT composites with the addition of only 40 wt.% in the paraffin matrix. In addition, the microwave absorption mechanism of the $BaTiO_3$@MWCNT core/shell heterostructure composites is proposed. The various polarizations including dielectric and interfacial polarization which originate from the heterogeneous structures and interfaces in the composites are responsible for their excellent microwave absorbing performances.

Keywords: $BaTiO_3$; MWCNTs; Heterostructure; Microwave absorption

1. Introduction

Recently, electromagnetic interference (EMI) from the widespread use of electronic devices has attracted a great deal of attention, prompting the exploration of effective electromagnetic wave absorbing materials (EMAMs) [1-3]. EMAMs are most popularly known for their ability to effectively reduce the radar cross-section of targets in the military, thereby contributing to stealth defense systems, but they also may be used to prevent potentially harmful human health effects [4]. To date, wide variety materials, including the conjugated polymers, dielectric, magnetic nanoparticles and their composites [5-10], have been used for microwave absorbing with a broad range of absorption bandwidth, well matched impedance and engineered geometries. Among them, Carbon-based materials with different structures, as well as their composites, including carbon black [11-13], carbon nanofibers [4], carbon nanotubes [14,15], and graphene [16], have attracted attention as EMAMs because they have good resistance against corrosion, high conductivity, variable morphology, superior mechanical strength and are lightweight [17-21].

Owing to their unique structure, multi-walled carbon nanotubes (MWCNTs) have interesting properties that make them good potential nanoscale building blocks with good foreground in the wave absorbing complex material domain [2,22]. Additionally, because MWCNTs have a structure that is on the nanoscale, the reflectivity of electromagnetic waves with much larger wavelengths (such as those used for radar) is greatly reduced, which contributes to the stealth

capabilities of the material. On the other hand, the high aspect ratio of MWCNTs provides a large interfacial area, which favors electron transport and electric conductivity. On the basis of EM transmission line theory, this can enhance their microwave absorption properties. To take advantage of these excellent structure and performances, MWCNTs have been utilized for the development of high performance microwave absorbing materials [14,23-26].

Extensive research has demonstrated that it is difficult to use single-component microwave absorbers to form highly efficient microwave absorbers. This is primarily because of the difficulty in obtaining an impedance match with a single system [27]. Furthermore, it is well known that the absorption properties of a material are closely related to its structure [28,29]. Recently, it has been found that one-dimensional hetero-nanostructures transition metal oxide/CNT composites exhibit great potential as broadband lightweight absorbers with lower reflection loss, due to the presence of two different functional materials and the resulting formation of heterojunctions at the interface. For instance, Song et al. [23] found that in ZnO/CNTs composites because the heterostructures widen the absorption band of the reflection-loss peaks, resulting in resonant absorption. Cao et al. [25] fabricated CNT-based heterostructures of Fe_3O_4/CNT composites and investigated their microwave absorption properties, demonstrating that the interfaces between the MWCNTs and the Fe_3O_4, and the heterostructures were playing an important role in the microwave absorption properties. Although there has been work done in this area, this topic still has room for improvement, such

as finding materials with good resistance against corrosion, understanding the influence of the heterojunction interface and synergetic effect, developing a lightweight absorber, and improving absorber performance. $BaTiO_3$ is also considered to be a good potential candidate for this application because of its high permittivity and a large propagation constant, which leads to a high attenuation constant. Considering the above advantages of $BaTiO_3$ and MWCNTs, the combination of both may result in the development of high performance microwave absorbers.

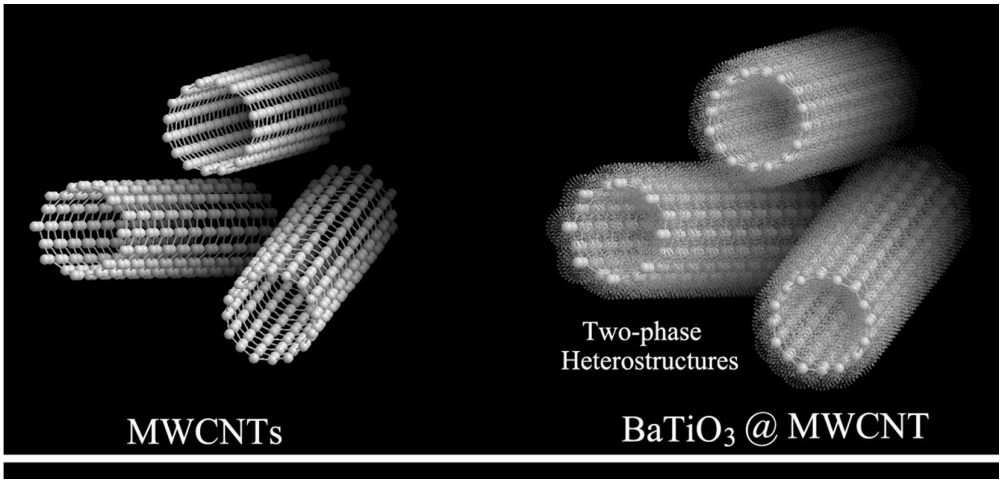

Figure 1. Illustrations of MWCNTs (left) and $BaTiO_3$@MWCNT composites (right)

Herein, we report a novel strategy for simple, effective and bulk scale synthesis of $BaTiO_3$@MWCNT core/shell heterostructure microwave absorbing composites by a sol-gel route combined with thermal treatment process. The cooperative combination of $BaTiO_3$ (dielectric shell) and MWCNTs (electrically conducting core), can offer advantages such as good electrical and dielectric properties which may collectively contribute to higher microwave absorption efficiency. Therefore，paraffin wax was selected as the host for the composites and separately embedded with single phase $BaTiO_3$, single phase MWCNTs (Fig. 1), and two phase

$BaTiO_3$@MWCNT (Fig. 1) to allow a direct comparison of their dielectric and microwave absorption properties. The implication of the comparison between single phase and two-phase heterostructures with respect to their potential applications in electromagnetic absorbing and attenuation performance is also discussed.

2. Experimental Section

2.1 Materials

MWCNTs with diameters ranging from 40 to 70 nm were obtained from the Wako Pure Chemical Reagent Co., Ltd., Japan. Oxidation of MWCNTs was carried out in hot, concentrated nitric acid. Barium acetate ($Ba(CH_3COO)_2$), tetraisopropyl titanate ($Ti(OC_3H_7)_4$), acetic acid and ethanol were supplied by Wako Pure Chemical Reagent Co., Ltd., Japan. All chemicals are used without further purification. Deionized water was used in all experiments.

2.2 Preparation of oxidized MWCNTs

Typically, MWCNTs (~0.5 g) were acidified by concentrated nitric acid with vigorous stirring for 6 h at 115°C, to obtain oxidized MWCNTs with a large number of oxygen-containing reactive groups on the ends and sidewall. The acid oxidized MWCNTs (AO-MWCNTs) were then collected by filtration and washed with deionized water until a neutral pH value was obtained in the washing solution.

2.3 Synthesis of $BaTiO_3$ precursors

The $BaTiO_3$ precursor was produced via a sol-gel method. The Ba and Ti cations were

controlled at a 1:1 molar ratio. In a typical process, barium acetate (5 mmol) was dissolved into a mixture of acetic acid (5 mL) and anhydrous ethanol (20 mL) with vigorous stirring for 30 min at 60 °C water bath, designated as solution A. Titanium isopropoxide (5 mmol) was dissolved into anhydrous ethanol (10 mL) containing deionized water (1 mL) with stirring for 15min to make it homogeneous. That solution then was added to the mixed solution A slowly under continuous stirring conditions and maintaining a temperature of 60 °C for 2 h, and then aged at room temperature for 24 h.

2.4 Synthesis of $BaTiO_3$@MWCNT composites

The $BaTiO_3$@MWCNT core/shell heterostructure composites were synthesized by a heat treatment method. In a typical fabrication experiment, the as-treated MWCNTs (100 mg) were dispersed in $BaTiO_3$ sol solution by ultrasonication for 30 min, and then vigorous stirring was applied to the mixture suspension for reaction at 40 °C for 4 h. The resulting suspension was filtered and the power was dried and then calcined in a tube furnace at 700 °C for 2h under high-purity Ar atmosphere. The obtained powder was sealed in bottles for further characterization. Pure $BaTiO_3$ particles were prepared using a similar synthesis procedure to that of the composite but absence of MWCNTs, and the sample of acid oxidized MWCNTs were used for comparison of the results.

2.5 Characterization

The morphology and microstructure of the products were characterized using field emission

scanning electron microscopy (FE-SEM; JEOL, Model S-5000) and transmission electron microscopy (TEM; JEOL, Model JEM-2010) with an accelerating voltage of 200 kV. The crystal structure of the prepared powders was analyzed with an X-ray diffractometer (RINT, Model 2550H), using Cu Kα radiation. The Raman spectroscopy investigation of the surface structural changes of the MWCNTs during treatment was performed with a HoloLab series 5000 Raman spectroscopy system (514 nm excitation of the laser). X-ray photoelectron spectroscopy (XPS; Kratos AXIS Ultra DLD) analysis was used to measure the chemical composition and chemical states of the samples. Thermogravimetric analysis (TGA) was carried out in air from room temperature to 700°C at a heating rate of 5°C/min using a TG8120 analyzer (Rigaku Denki).

The composite samples used for electromagnetic measurements were prepared by loading the products in paraffin wax. The powder-wax compound was then pressed into toroidally shaped samples (φ_{out} = 7mm, φ_{inner} = 3mm, $H_{thickness}$ = 2 mm) for complex permittivity ε ($\varepsilon=\varepsilon'-j\varepsilon''$) and permeability μ ($\mu=\mu'-j\mu''$) measurements with a vector network analyzer (37247D Anritsu Co., Ltd.) in the 0.5–15 GHz range, and the input power level was kept at -6 dBm.

3. Results and discussion

3.1 Morphology and structure analysis

Representative FE-SEM images of oxidized MWCNTs and $BaTiO_3$@MWCNT composites are shown in Fig. 2 (a–d). The neat oxidized MWCNTs morphology is displayed in Fig. 2 (a)

and (b) as endless, disentanglement, hollow ropes with smooth surfaces, with the diameter of each nanotube in the range of 40-70 nm. For the $BaTiO_3$@MWCNT composites, seen in Fig. 2 (c) and (d), a tubular layer of a highly uniformly coated film is clearly present on the oxidized MWCNTs surface and the surface is no longer smooth. It is also demonstrates that as-prepared composites have a homogeneous structure over the large scale and the diameter is ranges from 50-100 nm, which is larger than that of the oxidized MWCNTs.

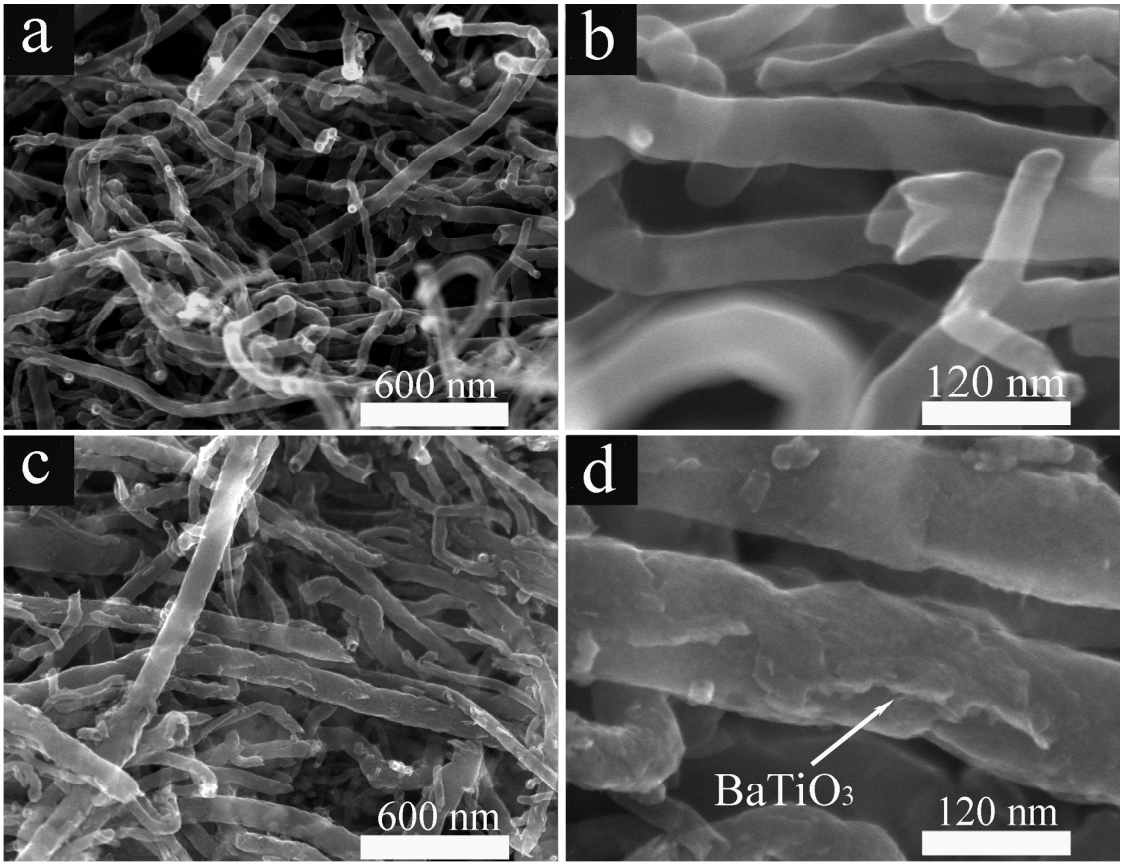

Figure 2. Representative FE-SEM images of MWCNTs (a) low magnification; (b) high magnification and $BaTiO_3$@MWCNT composites (c) low magnification; (d) high magnification.

Further structural characterization was performed by TEM, from which images of the $BaTiO_3$ @MWCNT composites at different resolutions are shown in Fig. 3 (a) and (b). Closer

inspection of TEM image, Fig. 3(a) reveals that the resulting $BaTiO_3$@MWCNT composites have a coaxially tubular structure. As is typical of core-shell structures the oxidized MWCNTs serve as the conducting core with the $BaTiO_3$ film uniformly encapsulated on the surface of the MWCNTs to form a tubular dielectric shell of fabricated composites. The tubular layer of coated $BaTiO_3$ film has a mean wall thickness of ~10 nm, as measured from TEM images, which is in accordance with the FE-SEM observations obtained from Fig. 2. The representatives high-resolution TEM image of the $BaTiO_3$@MWCNT composites in Fig. 3(b) reveals that $BaTiO_3$ film form a polycrystalline structure. The interplanar crystal spacing of ~ 0.285 nm is corresponds to the (110) crystalline plane of sample. The formation of the polycrystalline structure of $BaTiO_3$ may be induced by crystal structure of MWCNT with different orientation, which may lead to different growth orientation of grains and maintain the polycrystalline growth of $BaTiO_3$ during the heat treatment process. The selected-area electron diffraction pattern (SAED) of $BaTiO_3$@MWCNT composites, seen in the inset Fig.3 (b) shows distinct bright spots corresponding to characteristic planes of nanocrystalline $BaTiO_3$ (the $BaTiO_3$ unit cell parameters were obtained from JCPDS Power Diffraction File Card No. 31-0174); this is further confirmed by X-ray diffraction (XRD).

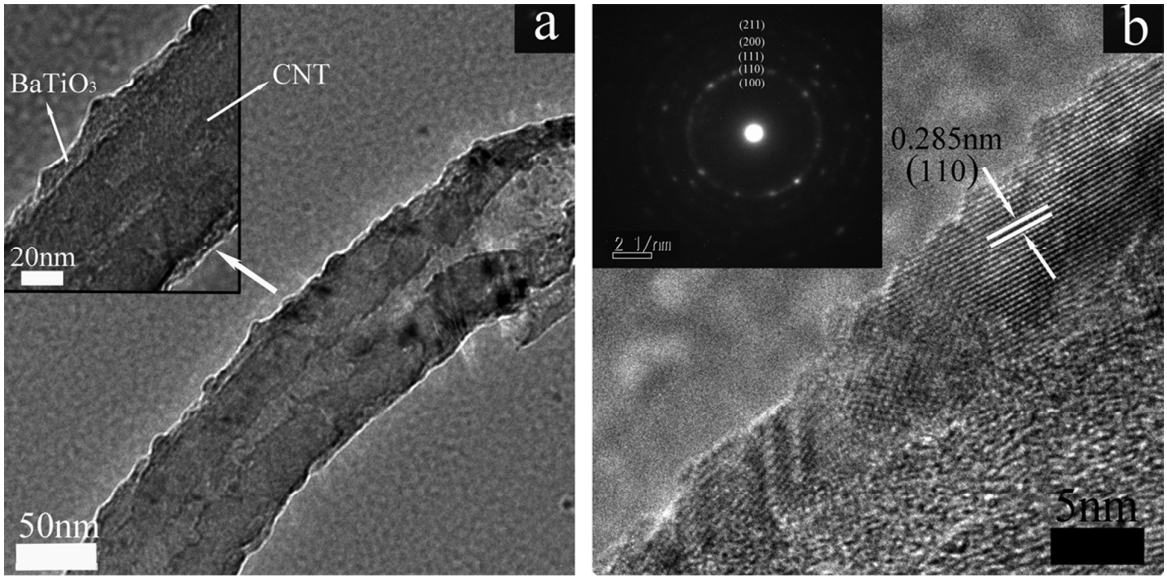

Figure 3. TEM images of the $BaTiO_3$@MWCNT composites at different resolutions (a, b). The inset in (b) is the corresponding electron diffraction pattern.

The crystalline phase and phase composition of the bare MWCNTs and the composites with $BaTiO_3$ were analyzed by XRD, as shown in Fig. 4. For the single phase MWCNTs, the diffraction peaks were observed at 26.2°, 42.77° and 53.6°, corresponding to the (002), (100), and (004) reflections of highly graphitized arc-discharge multiwalled nanotubes [25]. Meanwhile, a broad diffraction peak appearing at 2 theta ~22.2° originates from the (amorphous carbon) disordered graphite structure [30]. For the $BaTiO_3$@MWCNT composites, all of the diffraction peaks unaccounted for by the characteristic of the MWCNTs could be indexed to the cubic crystal structure of $BaTiO_3$; thus, there is no indication of crystalline byproducts, which matches well with the reported data (JCPDS Power Diffraction File Card No. 31-0174). Based on the XRD analyses, the c/a ratio for the sample is calculated to be about 1.0, well consistent with the standard value of cubic phase $BaTiO_3$ (1.0 from JCPDS Card: 31-0174). It is thus concluded that

the $BaTiO_3$@MWCNT core/shell heterostructure was formed. It is noted that the weak peak strength of the carbon nanotubes in the hybrid material is due to the high crystallinity of the $BaTiO_3$.

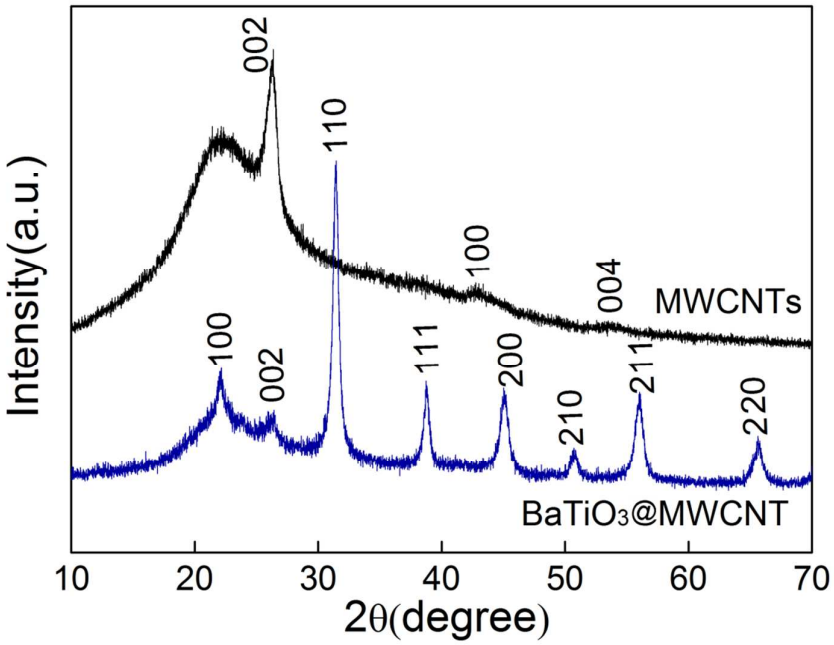

Figure 4. XRD pattern of MWCNTs and $BaTiO_3$@MWCNT composites

To well understand the formation process of $BaTiO_3$@MWCNT composites during the heat treatment, the compound particles of the precursor, $BaTiO_3$ xerogel/MWCNT, derived from the gel dried at 80 °C were thermally analyzed by TGA in N_2 atmosphere. Figure 5 shows the TGA curve of the oxidized MWCNTs and $BaTiO_3$ xerogel/MWCNT. As seen in Fig. 5(a), the TGA curve of oxidized MWCNTs shows that the weight loss (~5.26 %) is mainly related to the thermal degradation of the carboxyl and hydroxyl groups formed at the surface of the MWCNTs as well as a little loss of surface absorbed water at low temperature [31]. It is indicated that the MWCNTs are functionalized by nitric acid treatment, which is further confirmed by XPS. For

the $BaTiO_3$ xerogel/MWCNT, Fig. 5(b), it can be seen that three weight-loss steps take place over the scanning temperature range from 60 to 700 °C. The first weight loss (~5.64 %), from 60 to ~265 °C, is relatively gentle, and is related to the loss of volatile species, surface absorbed water and bound water molecules in the sample. The second weight loss step (~18.15%), between ~265 and 425 °C, is a relativlystep, and is caused by the decomposition of organic groups from the organometallic precursor and the formation of intermediate phases [32]. Then the steepest weight loss (~8.05 %) may be caused by the decomposition of the intermediate phases and the formation of $BaTiO_3$ in the range from 425 to 700 °C [33,34].

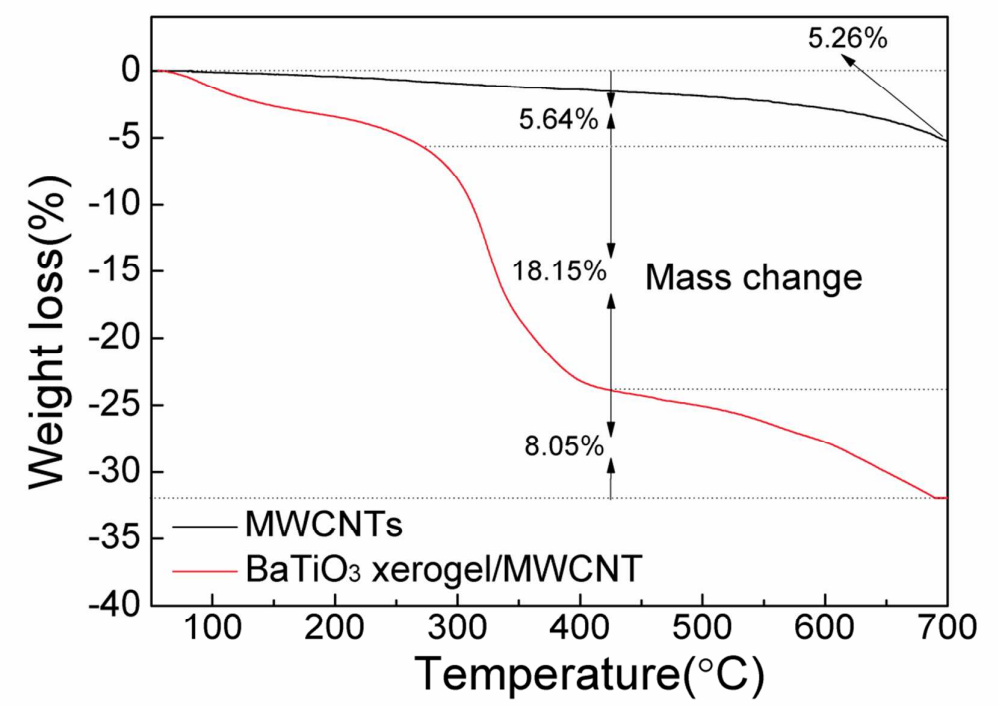

Figure 5. Thermogravimetric analysis of the $BaTiO_3$ xerogel/MWCNT

The XPS wide scan spectrum (Fig. 6) of raw-MWCNTs and AO-MWCNTs shows peaks corresponding to elemental of carbon (C1s) and oxygen (O1s). In addition, the relative

concentration O1s of AO-MWCNTs is higher than that of raw-MWCNTs, indicating that oxygen-containing functional groups have been successfully grafted to the surface of MWCNTs, consistent with the TGA analysis.

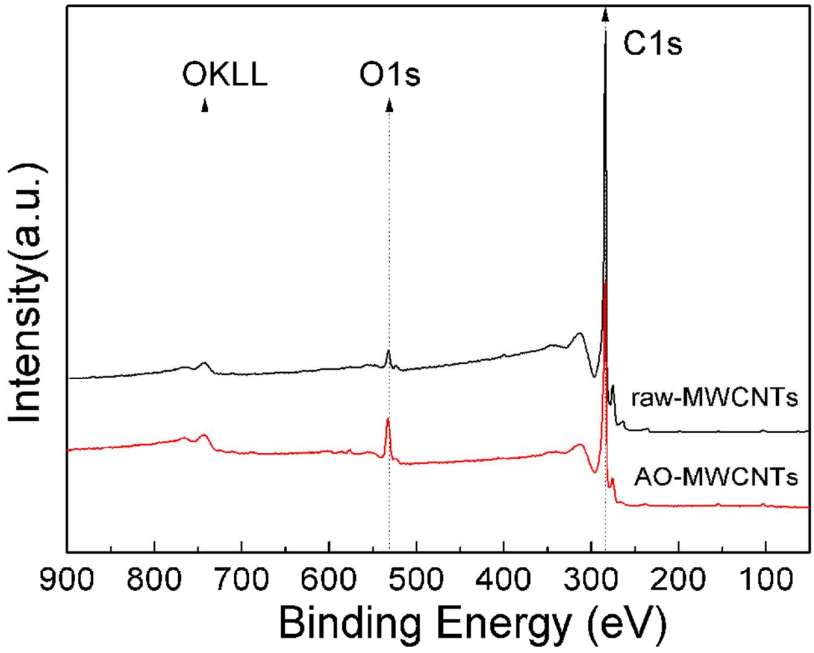

Figure 6. XPS wide scan of raw-MWCNTs and AO-MWCNTs

XPS was performed to verify the composition of the composites and confirm the chemical states of the elements. As seen in Fig. 7(a), survey scans of the sample identified the presence of carbon, barium, titanium, and oxygen. Notably, no other elements are detected, which led to the conclusion that a $BaTiO_3$@MWCNT heterostructure was formed. This finding is complemented by the FE-SEM, TEM and XRD results. In addition, the Ba:3d and Ti:2p core-level spectra of sample are shown in Fig. 7 (b) and (c). Ba:3d and Ti:2p appear to be a single chemical state. Also, the Ba:$3d_{5/2}$ and Ti:$2p_{3/2}$ binding energies measured for the composites were 779.0 and 458.9 eV, respectively, which are in excellent agreement with those reported in the literature

[35-37].

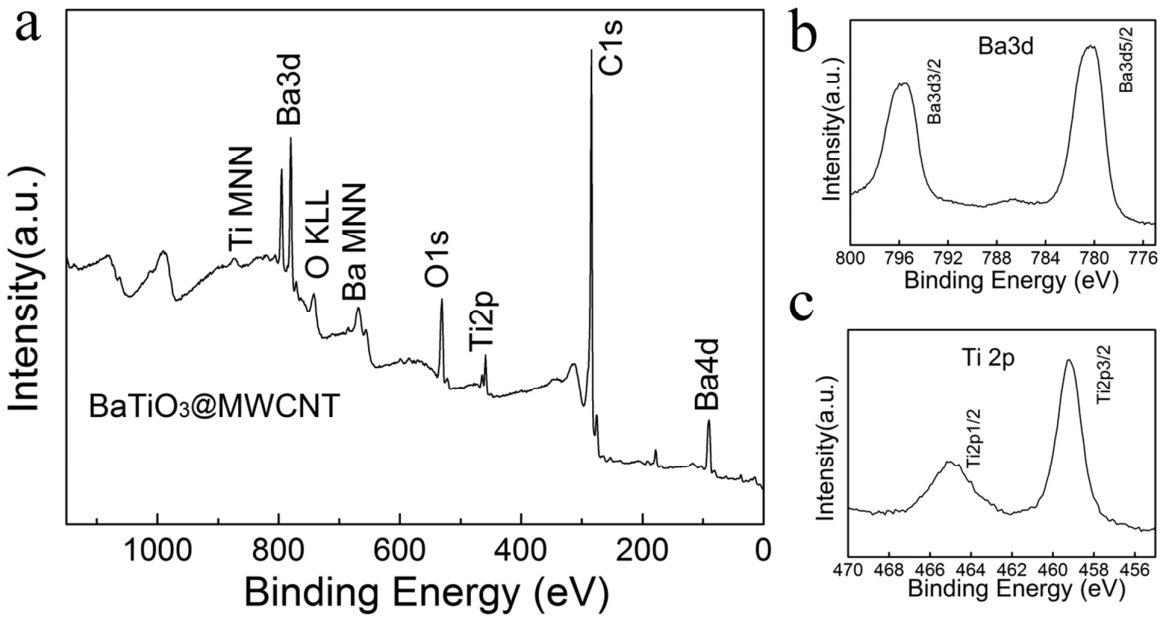

Figure 7. XPS spectra of (a) $BaTiO_3$@MWCNT composites; (b) Ba3d core-level spectrum and (c) Ti2p core-level spectrum

Raman spectroscopy is well known as a powerful tool for the characterization of carbon structures [38-41]. Raman spectroscopy has been used to study the structural changes of MWCNTs during the treatment, as shown in Fig. 8. The samples have similar Raman scattering patterns. The peak near 1343 cm^{-1} is assigned to the D-band, which corresponds to the disordered graphite structure coming from amorphous carbon and any defects [38,39,42]. The high frequency peak near 1571 cm^{-1} is the G-band; it originates from the tangential in-plane stretching vibrations of the carbon-carbon bands within the graphene sheets [34-36]. Furthermore, an additional Raman band at ~1610 cm^{-1} is the characteristic band of MWCNTs called the D' band, which is a double resonance Raman feature induced by disorder, defects or

ion intercalation between the graphitic wall [38-43]. The extent of the modification or defects in MWCNTs can be evaluated by the intensity ratio of the D and G band, I_D/I_G [42]. The intensity ratios of I_D/I_G are 0.84, 0.97, and 0.62 for raw-MWCNTs, AO-MWCNTs, and $BaTiO_3$@MWCNT, respectively. The intensity ratios I_D/I_G of AO-MWCNTs are higher than those of raw-MWCNTs, indicating that the functional groups to the defects have been grafted on to the MWCNTs [42]. As the $BaTiO_3$ films are coated on the MWCNTs, the intensity ratio of the I_D/I_G is decreased, suggesting that the $BaTiO_3$ films covered the defect sites [44]. Furthermore, the effect of high temperature treatment on the structural changes of MWCNTs was also investigated by Raman spectrum. The Raman spectrum of the HT-MWCNTs (as-received MWCNTs treated at 700 °C for 2h under Ar atmosphere) is similar to that of the as-received tubes, with a slightly lower I_D/I_G value of ~0.82, which indicates that the amorphous carbon layer at the MWCNT surface is removed without damaging the tubular structure of MWCNTs [42]. The structure of the $BaTiO_3$ film was further analyzed by Raman spectroscopy at the atomic scale on the basis of vibrational symmetry. Cubic $BaTiO_3$ inherently has no Raman-active modes, but such modes are expected for the noncentrosymmetric tetragonal structure [36]. The Raman spectrum of the $BaTiO_3$@MWCNT is shown in Fig.9. The dominant features in the sample Raman spectrum are a broad peak centered near 220 cm^{-1} [A_1(TO)], a weak peak at 302 cm^{-1} [B_1, E(TO+LO)], an asymmetric and broad peak at around 500 cm^{-1} [A_1, E(TO)] [45, 46]. The observed Raman peaks have been assigned to more than one phonon mode

implies that this phase does not have perfect cubic symmetry but has some disorder which

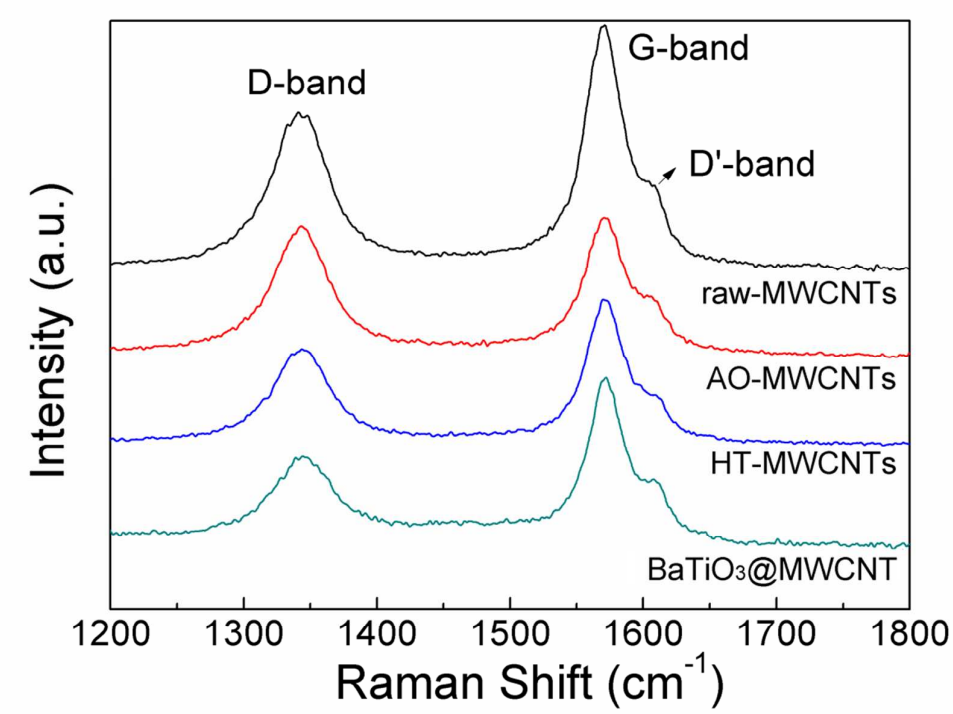

Figure 8. Raman spectrum of the samples

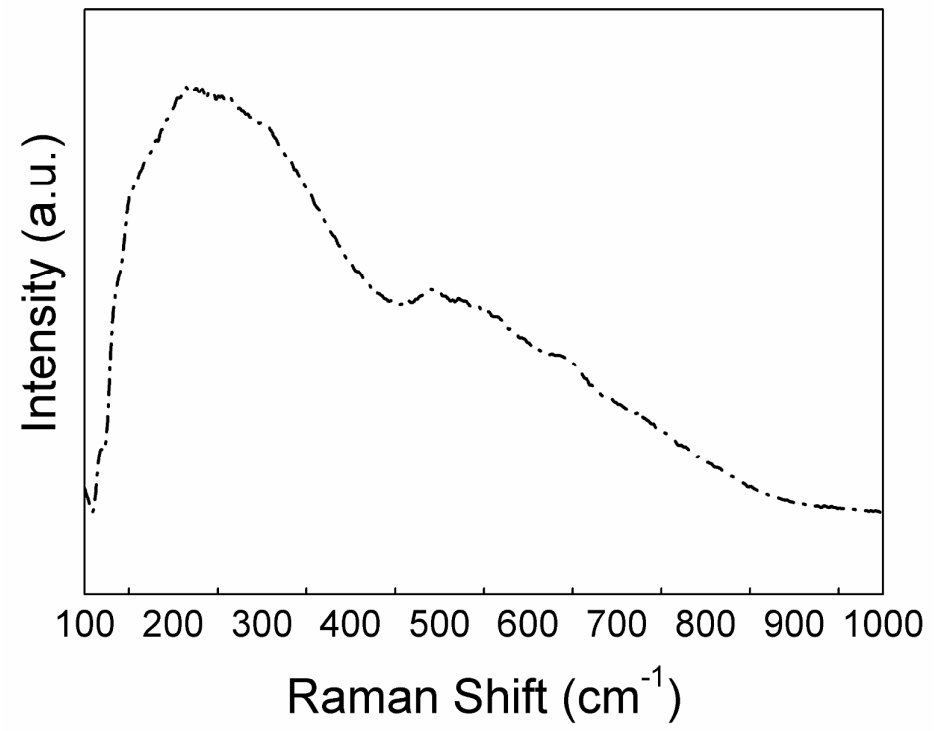

Figure 9. Raman spectrum of the $BaTiO_3$@MWCNT composites (focusing on the $BaTiO_3$ film)

breaks the symmetry and permits Raman activity. On the other hand, in polycrystalline material there are additional mechanisms such as grain boundaries and intergrain stresses that could break Raman selection rules [46]. Therefore, even though XRD analysis reveals a cubic perovskite structure, the observed Raman-active modes imply a certain degree of tetragonality on the atomic scale, in accordance with the previous report [36, 45].

3.2 Electromagnetic wave absorption properties of $BaTiO_3$@MWCNT composite

It is wellknown that the microwave absorption properties of an absorber are highly associated with its complex permittivity and complex permeability. Therefore, we independently measured the complex relative permittivity and permeability of these samples to get a better understanding of their microwave absorption properties. Fig.10 shows the real and imaginary parts of the complex relative permittivity (ε', ε'') and permeability (μ', μ'') measured for the three samples – single phase MWCNTs, single phase $BaTiO_3$ nanoparticles, and $BaTiO_3$@MWCNT composites – with 20 wt % loadings in paraffin wax. As shown in Fig.10 (a), it can be seen that the real parts of complex permittivity (ε') of the MWCNT- and the $BaTiO_3$@MWCNT-filled samples are markedly decreased with increasing frequency, whereas the ε' of the $BaTiO_3$ filled sample shows a very slow, steady decrease with increasing frequency. The phenomena can be attributed to the fact that the dipoles present in the material find it increasingly difficult to maintain the phase orientation with the electric vector of the incident radiation [47]. Further, the high electrical conductivity of the MWCNTs is indicative of a relatively high dipole density

(normalized polarons/bipolarons concentration), which cannot reorient themselves along with the applied electric field, and may responsible for observed rapidly decrease in ε' of MWCNT- and $BaTiO_3$@MWCNT-filled samples. As shown in Fig.10 (b), the imaginary part of the complex permittivity (ε'') of the samples remains almost constant throughout the entire frequency range, with some resonance peaks. It is also interesting to discover that the $BaTiO_3$@MWCNT-filled sample has a higher ε'' value than those of the MWCNT- and $BaTiO_3$-filled samples over the whole frequency range (with the notable exception of the sharp peak for MWCNT-filled sample in the low frequency range). This can be explained by the fact that the dielectric loss of the material is associated with the energy dissipation, which depends on different polarization mechanisms [48]. In this particular case, the dielectric loss of the $BaTiO_3$@MWCNT composites is related to both the orientational polarization and the space-charge polarization which are associated with the heterogeneity between the MWCNTs and the $BaTiO_3$. Therefore, it can be expected that the derived dielectric loss will effectively enhance the reflection loss of incident electromagnetic waves. Fig. 10 (c) and (d) show the variation of the real and imaginary parts, respectively, of the complex permeability of the samples with increasing frequency. For the complex permeability of the MWCNT-filled sample, both the real and imaginary parts showed strong fluctuations in the measured frequency. This phenomenon can be ascribed to the eddy currents that are induced by the electromagnetic waves because of the relatively high conductivity of the MWCNTs [49-50]. The real part μ' and

imaginary part μ'' of the $BaTiO_3$-filled sample show little change as a function of frequency and are nearly equal to 1 and 0, respectively. This indicates that the $BaTiO_3$-filled sample was unable to produce much magnetic loss. The real part μ' of $BaTiO_3$@MWCNT filled sample remains almost constant in the low frequency range and then gently increases with the increase of the frequency. Interestingly, the imaginary part μ'' of the $BaTiO_3$@MWCNT filled-sample behaves similarly with respect to frequency as that of real part μ'. The enhancement of the complex

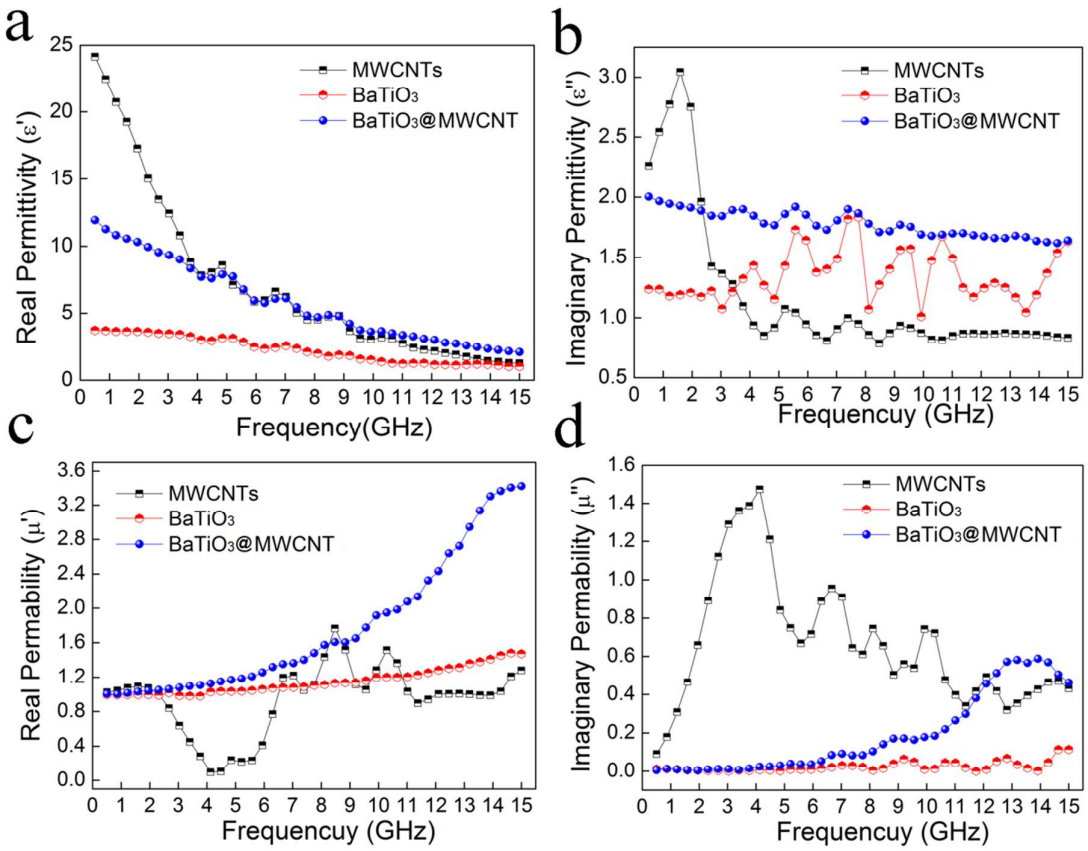

Figure 10. The (a) real part ε', (b) imaginary part ε'' of the complex permittivity and the (c) real part μ', (d) imaginary part μ'' of complex permeability for single phase MWCNTs, single phase $BaTiO_3$ and $BaTiO_3$@MWCNT composites with 20 wt% loadings in paraffin wax of 2 mm thickness in the frequency range of 0.5–15 GHz

permeability with increasing frequency can be explained as follows. Compared with the MWCNTs, the conductivity of the $BaTiO_3$@MWCNT composites will be lower because $BaTiO_3$ is an insulator; this then leads to a decrease of the number of eddy currents in system induced by the electromagnetic waves [49].

To further prove the dependence of the microwave absorption properties of the complex relative permittivity and permeability, the reflection loss (*RL*) properties of samples were calculated according to transmission line theory, as follows:

$$R.L. = 20\log\left|\frac{Z_{in}-1}{Z_{in}+1}\right| \qquad (1)$$

The normalized input impedance (Z_{in}) is given by the formula:

$$Z_{in} = \sqrt{\frac{\mu_r}{\varepsilon_r}}\tanh\left[j\left(\frac{2\pi fd}{c}\right)\sqrt{\mu_r\varepsilon_r}\right] \qquad (2)$$

where $\varepsilon_r=\varepsilon'-j\varepsilon''$, $\mu_r=\mu'-j\mu''$, f is the microwave frequency in Hz, d is the thickness of the absorber in m, and c is the velocity of light in free space in m/s. The calculated *RL* of the MWCNTs, $BaTiO_3$ and $BaTiO_3$@MWCNT with 20 wt. % loadings in paraffin wax are shown in Fig. 11. The dip of the curves designates the maximum *RL*, which means that either the reflection is at a minimum or the absorption is maximized at that particular point. It can be found that the reflection loss of $BaTiO_3$ nanoparticles is relatively weak and only shows a single peak at 15 GHz with value of -4.3 dB. As for the sample of MWCNTs, the microwave absorption is better than that of the $BaTiO_3$ nanoparticles, but the *RL* value is still larger than -7.4 dB. Very interestingly, a substantially enhanced microwave absorption performance can be observed in

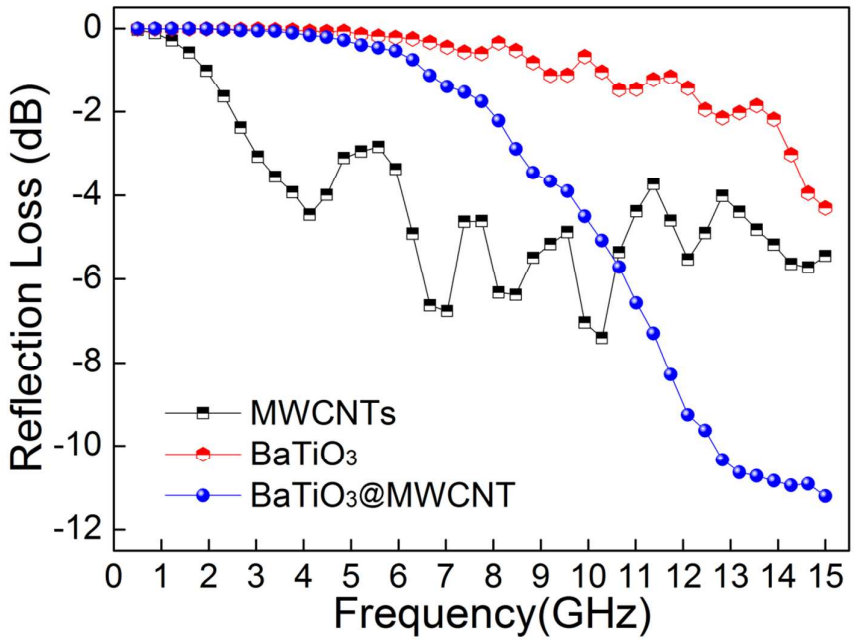

Figure 11. Reflection loss curves for MWCNTs, $BaTiO_3$ and $BaTiO_3$@MWCNT composites

the sample of $BaTiO_3$@MWCNT composites. It shows the maximum reflection loss of -11.2 dB (absorbing more than 90%) at 15 GHz and the frequency bandwidth is less than -10 dB from 12.8 to 15 GHz. Importantly, this means that the composites containing $BaTiO_3$@MWCNT composites (with 20 wt.% loading) can be used commercially as good wave absorbing materials. Of note is that the maximum reflection losses of the $BaTiO_3$ nanoparticles and MWCNTs are with 20 wt % loadings in paraffin wax of 2 mm thickness in the frequency range of 0.5–15 GHz. lower than that of the $BaTiO_3$@MWCNT composites. This may be caused by another important parameter of characteristic impedance, which is related to reflection loss [51,52]. Fig. 12 shows the reflection loss of mixtures of $BaTiO_3$@MWCNT composites and paraffin wax with different weight fractions that were obtained for sample thicknesses of 2 mm. The microwave absorbing

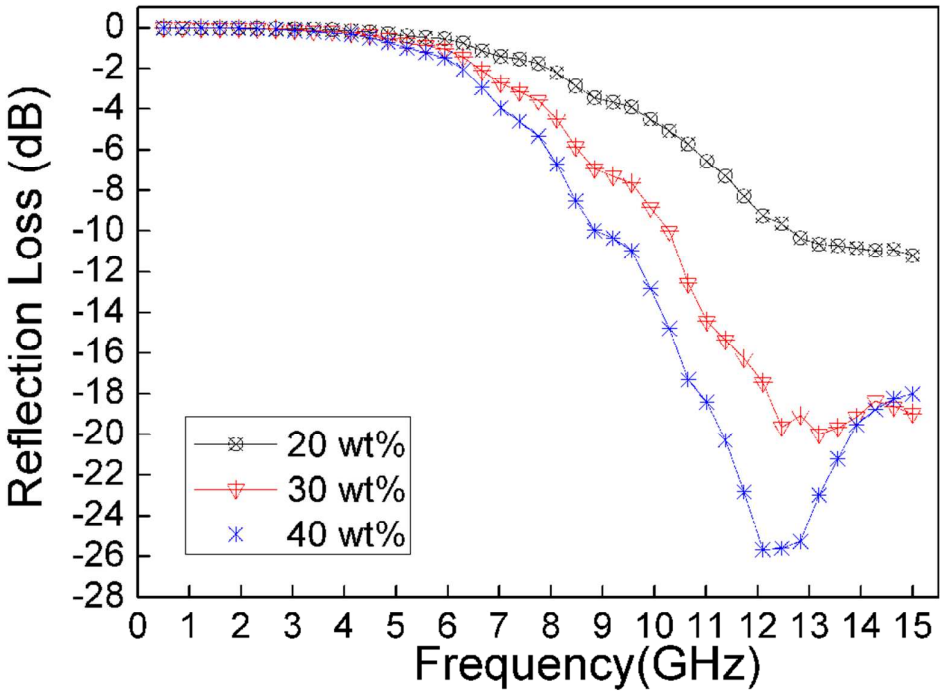

Figure 12. Reflection loss curves for different weight fractions of $BaTiO_3$@MWCNT/paraffin composite of the thickness of 2 mm in the frequency range 0.5–15 GHz

Table 1. Microwave absorption properties of samples.

Sample (weight fraction of $BaTiO_3$@MWCNT)	Microwave absorption properties of samples			
	***R.L.*$_m$ (dB)**	**f_m (GHz)**	**Frequency range (GHz) (*R.L.*<-10dB)**	**Frequency range (GHz) (*R.L.*<-20dB)**
20%	11.2	15.0	2.2	0
30%	20.0	13.2	4.7	One point
40%	25.7	12.1	5.8	2.5

$R.L._m$: minimum reflection loss value

f_m: frequency at which the reflection loss is at its minimum

parameters for the samples are listed in Table 1. It can be seen that the frequency for the maximum reflection loss increases as the loading percentage of fillers increases. The $BaTiO_3$@MWCNT/paraffin wax composite shows maximum reflection loss with value of -25.7 dB (~99.5% absorption) at 12.1 GHz for 40 wt%, and the frequency bandwidth less than -20dB

is from 11.3 to 13.8 GHz. To the best of our knowledge, this is comparatively large among the reported microwave absorption materials [53-57]. Moreover, it is also found that the maximum reflection loss is move slightly toward the low-frequency region as the filler weight fraction increased, which can be correlated with previous results [48, 58].

To get a better understanding of the microwave absorption ability difference in samples, the microwave absorption mechanism is proposed in Fig. 13. As seen in Fig.13 (a). Firstly, the high electrical conductivity of MWCNTs cannot cause considerable microwave absorption because most of the electromagnetic waves are reflected at the surface owing to the mismatched characteristic impedance. However, the MWCNTs covered with $BaTiO_3$ effectively decrease the electrical conductivity, leading to well matched characteristic impedances and fewer reflected electromagnetic waves, all of which enhances microwave absorption. In addition, the $BaTiO_3$@MWCNT composites are a heterogeneous system, where the behaviors of dielectric relaxation are made more complex by additional dielectric interfaces and more polarization charges on the interface between the $BaTiO_3$ and the MWCNTs [59]. Meanwhile, heterogeneous structures in the as-prepared nanocomposite also play important roles in the microwave absorption due to interfacial polarization [60]. Furthermore, the electrically conducting core of the MWCNTs can be repeatedly polarized; this allows them to act as dipoles that will be tuned with incident microwaves and contribute to strong absorption performance. As mentioned above, these are helpful for creating conditions whereby microwave energy is transformed to heat

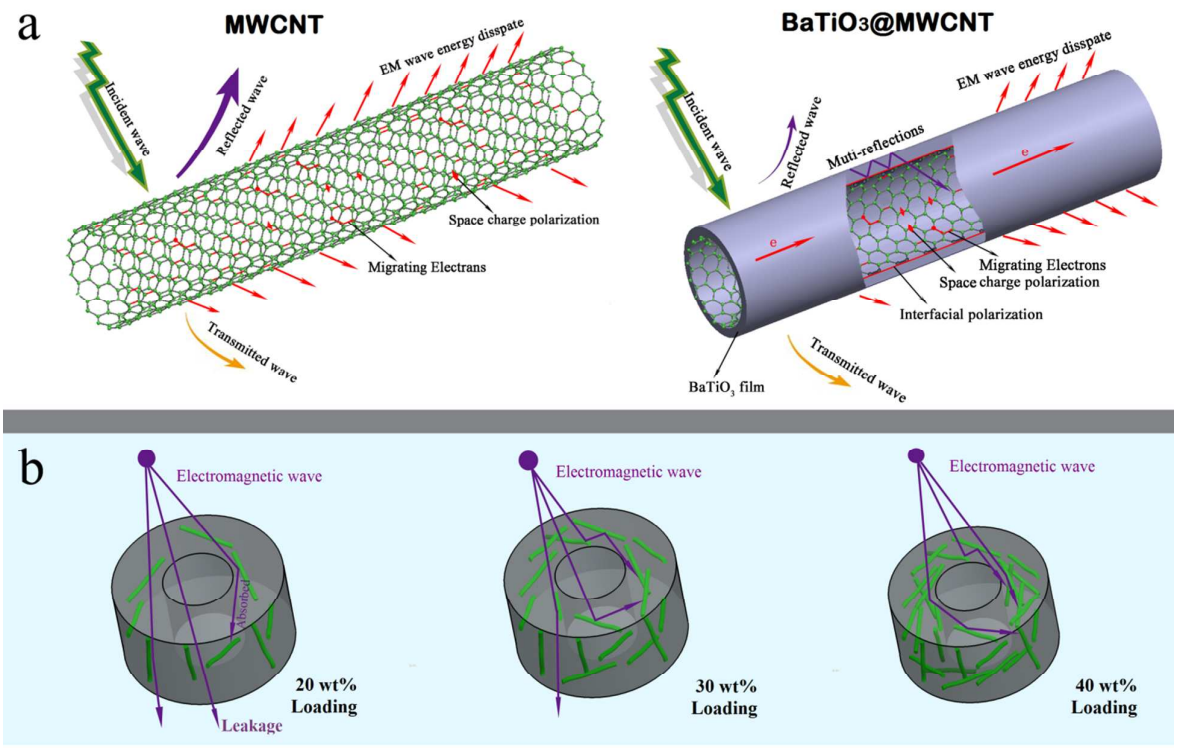

Figure 13. Possible mechanism for explaining the difference in microwave absorption by the prepared samples

energy (or other forms of energy) and finally dissipated. Accordingly, the enhancement of both the absorbing intensity and the bandwidth of the samples with increasing weight fraction could be explained with the help of Fig.13 (b). The probability of connectivity among the filler will increase with the increase in the loading of filler. Hence, the sample with the lowest porosity and the highest chances of connectivity among the filler (the sample with 40 wt% loading) will have the maximum absorption. Now, when the microwave radiation is incident on the samples, some part is absorbed and the remaining part is transmitted through the absorber. However, the microwave propagation paths in the absorbent will be more complex with increasing filler loading. Therefore, the leakage of radiation in the sample with 40 wt.% loading will be

minimized and the absorption will be maximied [48].

4. Conclusion

We have established the successful synthesis of $BaTiO_3$@MWCNT core/shell heterostructure composites via a sol-gel route combined with a thermal treatment process. The morphology, structure and formation process of $BaTiO_3$@MWCNTs composites were confirmed by FE-SEM, TEM, XRD, XPS, Raman spectroscopy and TGA. The $BaTiO_3$@MWCNT/paraffin wax composite showed the outstanding microwave absorbing performances, which were better than those of the individual components of the composites. Notably, more than 99% of electromagnetic wave energy could be attenuated by the $BaTiO_3$@MWCNT with an addition amount of only 40 wt.% in a paraffin matrix, and the frequency bandwidth less than -20 dB is from 11.3 to 13.8 GHz. The outstanding microwave absorbing performances are ascribed to dielectric and interfacial polarization arising from the heterogeneous structures of the composites and interfaces between the $BaTiO_3$ and MWCNTs. Thus, these high performance microwave attenuation behaviors provide valuable information for the exploration and development of advanced microwave attenuation materials in industry.

Acknowledgments

This research was supported by Zhejiang Provincial Natural Science Foundation of China (No. LQ14E030010); Zhejiang Top Priority Discipline of Textile Science and Engineering (No. 2013YBZX04); The Young Researchers Foundation of Key Laboratory of Advanced Textile

Materials and Manufacturing Technology, Ministry of Education, Zhejiang Sci-Tech University (No.2013QN07); Science Foundation of Zhejiang Sci-Tech University (ZSTU) (Nos. 13012147-Y and 13012062-Y).

References

[1] J. C. Wang, H. Zhou, J. D. Zhuang and Q. Liu. *Sci. Rep.*, 2013, **3**, 3252.

[2] M. Zong, Y. Huang, H. W. Wu, Y. Zhao, S. Q. Wang, N. Zhang and W. Zhang. *Mater. Lett.*, 2013, **111**, 188.

[3] C. L. Zhu, M. L. Zhang, Y. J. Qiao, G. Xiao, F. Zhang and Y. J. Chen. *J. Phys. Chem. C*, 2010, **114**, 16229.

[4] G. Li, T. S. Xie, S. L. Yang, J. H. Jin and J. M. Jiang. *J. Phys. Chem. C*, 2012, **116**, 9196.

[5] P. Saini, V. Choudhary, B. P. Singh, R. B. Mathur and S. K. Dhawan. Mater. Chem. Phys., 2009, **113**, 919.

[6] P. Saini, V. Choudhary, B. P. Singh, R. B. Mathur and S. K. Dhawan. Synth. Met., 2011, **161**, 1522.

[7] P. Saini and M. Arora. De Souza Gomes, A., Ed., InTech: Croatia, 2012.

[8] P. Saini and V. Choudhary. J. Nanopart. Res., 2013, **15**, 1415.

[9] P. Saini, V. Choudhary, N. Vijayan and R.K. Kotnala, J. Phys. Chem. C, 2012, **116**, 13403.

[10] S. M. Abbas, R. Chattterjee, A. K. Dixit, A. V. R. Kumar, T. C. Goel. J. Appl. Phys., 2007, **101**, 074105.

[11] M. H. Al-Saleh, W. H. Sadaah and U. Sundararaj. *Carbon*, 2013, **60**, 146.

[12] J. H. Oh, K. S. Oh, C. G. Kim and C. S. Hong. *Compos. Part B Eng.*, 2004, **35**, 49.

[13] X. X. Liu, Z. Y. Zhang and Y. P. Wu. *Compos. Part B Eng.*, 2011, **42**, 326.

[14] B. Wen, M. S. Cao, L. Z. Hou, W. L. Song, L. Zhang, M. M. Lu, H. B. Jin, X. Y. Fang, W. Z. Wang and J. Yuan. *Carbon*, 2013, **65**, 124.

[15] N. Li, Y. Huang, F. Du, X. B. He, X. Lin, H. J. Gao, Y. F. Ma, F. F. Li, Y. S. Chen and P. C. Eklund. *Nano. Lett.*, 2006, **6**, 114.

[16] P. B. Liu, Y. Huang and X. Sun. *ACS Appl. Mater. Inter.*, 2013, **5**, 12355.

[17] J. Zhang, J. W. Liu, C. Y. Liang, F. Zhang and R. C. Che. *J. Alloy. Compd.*, 2013, **548**,13.

[18] J. W. Liu, J. Cheng, R. C. Che, J. J. Xu, M. M. Liu and Z. W. Liu. *J. Phys. Chem. C*, 2013, **117**, 489.

[19] J. W. Liu, R. C. Che, H. J. Chen, F. Zhang, F. Xia, Q. S. Wu, and M. Wang. *Small*, 2012, **8**, 1214.

[20] C. S. Li, D. Z. Wang, X. F. Wang and J. Liang. *Carbon*, 2005, **43**, 1557.

[21] J. W. Liu, J. J. Xu, R. C. Che, H. J. Chen, Z. W. Liu and F. Xia. *J. Mater. Chem.*, 2012, **22**, 9277.

[22] Q. H. Li and X. L. Liu. *Appl. Phys. Res.*, 2010, **2**, 185.

[23] W. L. Song, M. S. Cao, B. Wen, Z. L. Hou, J. Cheng and J. Yuan. *Mater. Res. Bull.*, 2012, **47**, 1747.

[24] Q. Huang and L. Gao. *J. Mater. Chem.*, 2004, **14**, 2536.

[25] M. S. Cao, J. Yang, W. L. Song, D. Q. Zhang, B. Wen, B. H. Jin, Z. L. Hou and J. Yuan. *ACS Appl. Mater. Inter.*, 2012, **4**, 6949.

[26] Z. J. Wang, L. N. Wu, J. G. Zhou, W. Cai, B. Z. Shen and Z. H. Jiang. *J. Phys. Chem. C*, 2013, **117**, 5446.

[27] N. Joseph, S. K. Singh, R. K. Sirugudu, V. R. K. Murthy, S. Ananthakumar and M. T. Sebastian. *Mater. Res. Bull.*, 2013, **48**, 1681.

[28] H. F. Li, Y. H. Huang, G. B. Sun, X. Q. Yan, Y. Yang, J. Wang and Y. Zhang. *J. Phys. Chem. C*, 2010, **114**, 10088.

[29] X. S. Qi, Y. Deng, W. Zhong, Y. Yang, C. Qin, C. Au and Y. W. Du. *J. Phys. Chem. C*, 2010, **114**, 808.

[30] Y. L. Ren, C. L. Zhu, S. Zhang, C. Y. Li, Y. J. Chen, P. Gao, P. P. Yang and Q. Ouyang. *Nanoscale*, 2013, **5**, 12296.

[31] T. M. Wu and W. Y. Lin. *Polymer*, 2006, **47**, 3576.

[32] D. Y. Lee, H. M. Lee, N. I. Cho, B. Y. Kim and Y. J. Oh. *Met. Mater. Int.*, 2010, **16**, 453.

[33] L. N. Jing, G. Q. Wang, Y. P. Duan and Y. Z. Jiang. *J. Alloys. Compd.*, 2009, **475**, 862.

[34] G. Q. Wang, X. D. Chen, Y. P. Duan and S. H. Liu. *J. Alloys. Compd.*, 2008, **454**, 340.

[35] R. L. Brutchey and D. E. Morse. *Angew. Chem.*, 2006, **118**, 6714.

[36] Y. F. Zhu, L. Zhang, T. Natsuki, Y. Q. Fu and Q. Q. Ni. *ACS Appl. Mater. Inter.*, 2012, **4**,

2101.

[37] Y. F. Zhu, Y. Q. Fu, T. Natsuki, Q. Q. Ni. Polym. Compos., 2013, **34**, 265.

[38] A. Jorio, R. Saito, G. Dresselhaus, M. S. Dresselhaus. *Phil. Trans. R. Soc. Lond. A* 2004, **362**, 2311.

[39] M. S. Dresselhaus, G. Dresselhaus, R. Saito, A. Jorio. *Phys. Rep.*, 2005, **409**, 47.

[40] A. M. Rao, E. Richter, S. J. Bandow, B. Chase, P. C. Eklund, K. A. Williams, S. Fang, K. R. Subbaswamy, M. Menon, A. Thess, R. E. Smalley, G. Dresselhaus and M. S. Dresselhaus. *Science*, 1997, **275**, 187.

[41] C. Thomsen, S. Reich and J. Maultzsch. *Phil. Trans. R. Soc. Lond. A*, 2004, **362**, 2337.

[42] S. Osswald, M. Havel and Y. Gogotsi. *J. Raman Spectrosc.*, 2007, **38**, 728.

[43] X. L. Zhao, Y. Ando. *Jpn. J. Appl. Phys.*, 1998, **37**, 4846.

[44] S. Y. Wang, S. P. Jiang and X. Wang. *Nanotechnology*, 2008, **19**, 265601.

[45] R. L. Brutchey, and D. E. Morse. Angew. Chem., 2006, **118**, 6714.

[46] U. D. Venkateswaran, V. M. Naik, and R. Naik. Phys. Rev. B, 1998, **58**, 14256

[47] P. Saini, M. Arora, G. Gupta, K. B. Gupta, V. N. Singh, V. Choudhary. *Nanoscale*, 2013, **5**, 4330.

[48] B. Pallab, and K. D. Chapal. *Ind. Eng. Chem. Res.*, 2013, **52**, 9594.

[49] X. G. Liu, B. Li, D. Y. Geng, W. B. Cui, F. Yang, Z. G. Xie, D.J. Kang and Z.D. Zhang. *Carbon*, 2009, **47**, 470.

[50] C. Bi, Zhu MF, Q. H. Zhang, Y. G. Li, H. Z. Wang. *J. Nanosci. Nanotechno.*, 2011, **11**,

1030.

[51] P. Xu, X. J. Han, C. Wang, D. H. Zhou, Z. S. Lv, A. H. Wen, X. H. Wang and B. Zhang. *J. Phys. Chem. B*, 2008, **112**, 10443.

[52] L. Du, Y. C. Du, Y. Li, J. Y. Wang, C. Wang, X. H. Wang, P. Xu, and X. J. Han. *J. Phys. Chem. C*, 2010, **114**, 19600.

[53] N. Li, M. H. Cao, C. W. Hu. *J. Mater. Chem.*, 2012, **22**, 18426.

[54] R. C. Che, L. M. Peng, X. F. Duan, Q. Chen and X. L. Liang. *Adv. Mater.*, 2004, **16**, 401.

[55] Q. L. Liu, D. Zhang, and T. X. Fan. *Appl. Phys. Lett.*, 2008, **93**, 013110.

[56] T. Chen, F. Deng, J. Zhu, C. Chen, G. Sun, S. Ma and X. Yang. *J. Mater. Chem.*, 2012, **22**, 15190.

[57] C. Wang, X. Han, P. Xu, J. Wang, Y. Du, X. Wang, W. Qin and T. Zhang. *J. Phys. Chem. C*, 2010, **114**, 3196.

[58] Y. C. Qing, W. C. Zhou, F. Luo and D. M. Zhu. *J. Magn. Magn. Mater.*, 2009, **321**, 25.

[59] J. Cao, W. Y. Fu, H. B. Yang, Q. J. Yu, Y. Y. Zhang, S. K. Liu, P. Sun, X. M. Zhou Y. Leng, S. M. Wang, B. B. Liu and G. T. Zou. *J. Phys. Chem. B*, 2009, **113**, 4642.

[60] H. L. Zhu, Y. J. Bai, R. Liu, N. Lun, Y. X. Qi, F. D. Han and J. Q. Bi. *J. Mater. Chem.*, 2011, **21**, 13581.

Figure captions:

Figure 1. Illustrations of MWCNTs (left) and $BaTiO_3$@MWCNT nanocomposites (right)

Figure 2. Representative FE-SEM images of MWCNTs at (a) low magnification, and (b) high magnification and of $BaTiO_3$@MWCNT nanocomposites at (c) low magnification, and (d) high magnification.

Figure 3. TEM images of the $BaTiO_3$@MWCNT nanocomposites at different resolutions (a, b). The inset in (b) is the corresponding electron diffraction pattern.

Figure 4. XRD pattern of MWCNTs and $BaTiO_3$@MWCNT nanocomposites.

Figure 5. Thermogravimetric analysis of the $BaTiO_3$ xerogel/MWCNT.

Figure 6. XPS wide scan of raw-MWCNTs and AO-MWCNTs.

Figure 7. XPS spectra of (a) $BaTiO_3$@MWCNT nanocomposites; (b) Ba:3d core-level spectrum and (c) Ti:2p core-level spectrum.

Figure 8. Raman spectrum of the samples.

Figure 9. Raman spectrum of the $BaTiO_3$@MWCNT composites (focusing on the $BaTiO_3$ film)

Figure 10. The (a) real part ε', and (b) imaginary part ε'' of the complex permittivity and the (c) real part μ', and (d) imaginary part μ'' of complex permeability for single phase MWCNTs, single phase $BaTiO_3$ and $BaTiO_3$@MWCNT nanocomposites with 20 wt.% loadings in paraffin wax of 2 mm thickness in the frequency range of 0.5–15 GHz.

Figure 11. Reflection loss curves for MWCNTs, $BaTiO_3$ and $BaTiO_3$@MWCNT

nanocomposites with 20 wt. % loadings in paraffin wax of 2 mm thickness in the frequency range of 0.5–15 GHz.

Figure 12. Reflection loss curves for different weight fractions of $BaTiO_3$@MWCNT/paraffin composite of a thickness of 2 mm in the frequency range 0.5–15 GHz

Figure 13. Possible mechanism for explaining the difference in microwave absorption by the prepared samples.

Graphical Abstract

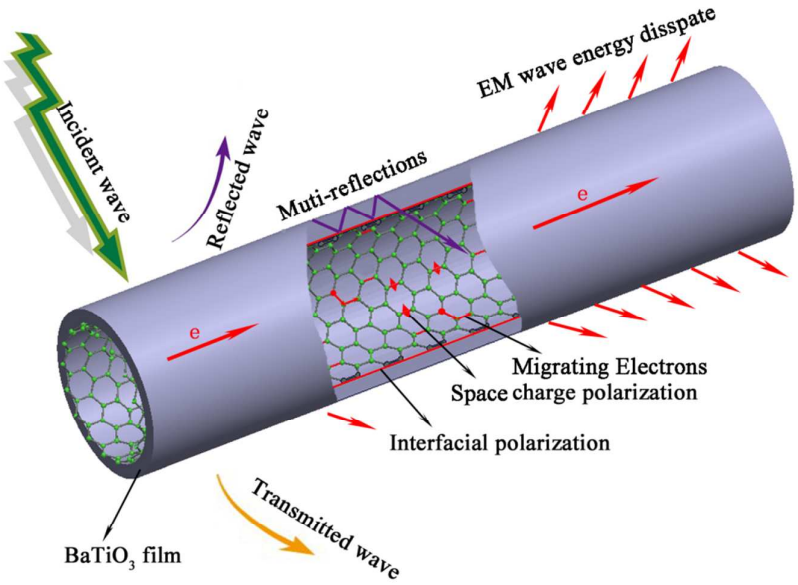

One-dimensional $BaTiO_3$@MWCNT with core/shell heterostructures have been explored as the electromagnetic microwave absorbers, which showed the maximum reflection loss with value of -25.7 dB (~99.5% absorption) at 12.1 GHz for 40 wt% loadings in paraffin wax, and the frequency bandwidth less than -20dB is from 11.3 to 13.8 GHz.